

Flux Pumped Kerr-Free Parametric Amplifier

Kagan Yanik,^{1,2} Irwin Huang,^{1,2} Bibek Bhandari,^{2,*} Bingcheng Qing,³ Ahmed Hajj,^{3,4} Ke Wang,³ David I Santiago,^{3,5} Irfan Siddiqi,^{3,5} Justin Dressel,^{6,2} and Andrew N Jordan^{7,6,2,1}

¹*Department of Physics and Astronomy, University of Rochester, Rochester, NY 14627, USA*

²*Institute for Quantum Studies, Chapman University, Orange, CA 92866, USA*

³*Quantum Nanoelectronics Laboratory, Department of Physics,
University of California at Berkeley, Berkeley, CA 94720, USA*

⁴*Graduate Group in Applied Science and Technology, University of California at Berkeley, Berkeley, CA 94720, USA*

⁵*Computational Research Division, Lawrence Berkeley National Laboratory, Berkeley, Berkeley, CA 94720, USA*

⁶*Schmid College of Science and Technology, Chapman University, Orange, CA 92866, USA*

⁷*The Kennedy Chair in Physics, Chapman University, Orange, CA 92866, USA*

We propose a flux-pumped superconducting parametric amplifier based on symmetrically threaded superconducting quantum interference devices (SQUIDs) that achieves a Kerr-free operating point under suitable drive conditions. Eliminating the Kerr nonlinearity is advantageous for quantum-limited amplification, as it mitigates unwanted distortions in squeezing and prevents degradation of both gain and quantum efficiency in the high-gain strong drive regime. By replacing the central junction in the symmetrically threaded SQUIDs (STS) configuration with a linear inductor, we find that the Kerr nonlinearity can be eliminated and the effective Hamiltonian reduces to that of a degenerate parametric amplifier (DPA), up to higher-order corrections in the zero-point fluctuations of the superconducting phase operator. We show that the deviations from ideal DPA behavior introduced by these higher-order terms are significantly weaker than those associated with a Kerr nonlinearity. Consequently, the STS design can be driven strongly while maintaining near-quantum-limited performance at the Kerr-free point. Our analysis predicts phase-preserving gain and efficiency approaching the quantum limit, with robust operation demonstrated up to 25 dB of gain.

Introduction— Superconducting qubits have emerged as leading candidates for achieving scalable, fault-tolerant quantum processors [1–10]. The accuracy of quantum algorithms and error correction in these devices, however, rely heavily on fast, high-fidelity single-shot measurement of the qubit states [4–7, 11]. This has driven research for the development of high-gain and high-efficiency microwave parametric amplifiers for superconducting qubit readouts [12–17]. These devices rely on wave-mixing processes, where a high-frequency pump interacts with a low-frequency signal via a nonlinear medium, transferring energy to amplify the signal. Parametric amplifiers can operate either in the phase preserving [18–23] or phase sensitive mode [14, 24–26]. In this letter, we focus on phase-preserving parametric amplifiers which amplify both quadratures symmetrically and can provide phase-independent quantum-limited amplification suitable for multi-qubit readout [5, 7, 27].

Josephson parametric amplifiers (JPAs) are widely used to achieve near quantum-limited phase preserving amplification in superconducting qubit readout [7, 27, 28]. JPAs can be operated using two pumping schemes: current pumping and flux pumping. In the current-pumping scheme, the intrinsic nonlinearity of the Josephson junctions is exploited to directly modulate the current through the device, typically by driving the pump at the same frequency as the cavity resonance frequency [29–32]. However, current pumping suffers from two major drawbacks. First, the pump and output signal share the same port and same frequency, making it difficult to separate them [14, 33, 34]. Pump leakage into the output path adds unwanted noise beyond the minimum allowed by quantum mechanics, necessitating additional filtering and complicating the path to quantum-limited performance [14, 29].

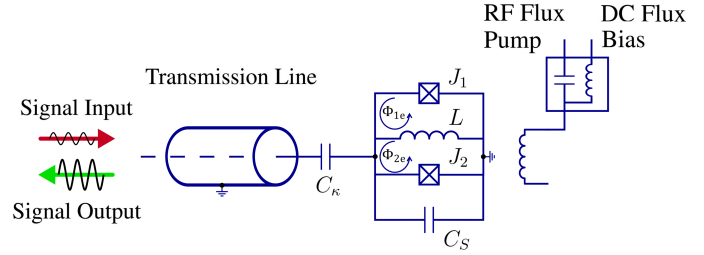


FIG. 1. Circuit of a lossless lumped-element flux-pumped Kerr-free STS amplifier coupled to a transmission line propagating the signal input and output fields. The outer branches are composed of junctions J_1 and J_2 whereas the middle branch consists of an inductor L . The double SQUID loop is shunted by a capacitor C_S and threaded by an external flux consisting of dc flux bias and ac flux modulation via pump line inductively coupled to the STS. The loop between $J_{1(2)}$ and L is threaded by an external flux $\Phi_{1(2)e}$.

Bichromatic current pumping was also explored in Ref. [14], where two far detuned current pumps are applied such that their combined frequency equals twice the cavity resonance frequency. This approach provides spectral separation between the pump and signal, allowing the pump tones to be filtered out before measurement. Nevertheless, this scheme still induces a pump-dependent shift of the cavity resonance frequency. Second, the current pump induces a large shift in the cavity resonance frequency [14] resulting in a higher parametric threshold for maximum gain. In contrast, flux pumping modulates the effective inductance of the JPA by varying the magnetic flux threading the dc superconducting quantum interference devices (SQUID) loop [14, 35, 36]. This scheme overcomes the limitations of current pumping since (i) the

pump and signal naturally couple to different physical ports, which strongly suppresses pump leakage and reduces added noise [14, 29, 35, 37], and (ii) flux-pumping produces a much smaller cavity detuning compared to current pumping [14].

In many previous studies, JPAs have been treated as ideal quantum-limited amplifiers, with higher-order nonlinear effects neglected [14]. However, Refs. [14, 38, 39] demonstrate that these higher-order corrections introduce nonidealities that degrade JPA performance, leading to deviations from the quantum limit in the high-gain regime and imposing constraints on the saturation power. The dominant source of these deviations is the Kerr nonlinearity [40]. Near-quantum-limited operation in the Kerr-free regime has been achieved in current-pumped amplifiers based on superconducting nonlinear asymmetric inductive element (SNAIL) [40–43] and Josephson parametric converter with an inductively shunted Josephson ring modulator (JRMs) [27]. These amplifiers employ a three-wave current pumping scheme which provides a large spectral separation of signal and pump. However, to our knowledge, an analogous Kerr-free implementation based on flux pumping has not yet been demonstrated.

In this letter, we propose the Symmetrically Threaded SQUIDs (STS) architecture, introduced in Ref. [44], as a flux-pumped platform for realizing a Kerr-free amplifier operating near the quantum limit. In our implementation, the Josephson junction in the central branch of the STS [44] is replaced by a linear inductor, which cancels the Kerr nonlinearity of the device for a particular static drive. A comparable design, referred to as linear inductive coupler (LINC) in Ref. [45], has been used as a nonlinear coupling element that remains essentially linear when idle and activates its nonlinearity only under drive to implement gates. We first analyze the higher order nonidealities of conventional single-loop flux-pumped dc SQUID amplifiers and establish that Kerr nonlinearity is the dominant nonideality that needs to be mitigated to approach quantum limited amplification. Since Kerr nonideality cannot be completely canceled in single-loop SQUID amplifiers, we propose the STS amplifier design as a solution to operating at Kerr-free regime. We find that the STS amplifier achieves phase-preserving gain and quantum efficiency that closely match those of an ideal degenerate parametric amplifier (DPA), demonstrating near-quantum-limited performance. In addition, our gain and efficiency analysis shows that the Kerr-free STS design surpasses conventional flux-pumped JPAs based on a single-loop dc SQUID, whose operation is constrained by Kerr-induced nonidealities.

Ideal quantum-limited amplifiers— Ideal quantum-limited microwave amplifiers are often modeled after the degenerate parametric amplifier (DPA), which consists of a single-mode cavity containing a nonlinear medium and is pumped at twice its resonance frequency through a two-photon squeezing drive [16, 18]. In its ideal form, the DPA Hamiltonian includes only the harmonic oscillator term and the two-photon squeezing interaction

$$\hat{H}_{\text{DPA}} = \Delta \hat{a}^\dagger \hat{a} + \frac{\lambda}{2} \hat{a}^{\dagger 2} + \frac{\lambda^*}{2} \hat{a}^2, \quad (1)$$

where \hat{a} (\hat{a}^\dagger) denotes the intracavity field annihilation (creation) operator, the detuning $\Delta = \omega_a - \omega_p/2$, ω_a is the cavity resonance frequency, ω_p is the pump frequency, and λ is the two-photon drive strength. Phase-preserving DPAs operate at the quantum limit when cavity dissipation stems solely from the coupling strength of the input signal [14]. The phase-preserving DPA gain is given by [14, 31]

$$G_{\text{DPA}} = \left| \frac{\kappa \bar{\kappa}/2 - i\kappa(\Delta + \omega)}{\Delta^2(\bar{\kappa}/2 - i\omega)^2 - |\lambda|^2} - 1 \right|^2, \quad (2)$$

where $\omega = \omega_s - \omega_p/2$, ω_s is the signal frequency, $\bar{\kappa} = \kappa + \gamma$ is the total damping rate of the cavity, κ is the coupling rate of the signal to the cavity, and γ is the coupling rate of additional noises to the cavity addressing the undesired losses [14, 18]. DPA is quantum-limited when there are no undesired losses ($\gamma = 0$) [14]. Moreover, the gain diverges at the parametric threshold $\lambda_{\text{crit}} = \sqrt{\Delta^2 + \bar{\kappa}^2/4}$ [14, 46, 47]. Hence, the amplifier needs to be operated at a value smaller than but near λ_{crit} for high gain.

Flux-pumped SQUID-based architectures— Efforts to realize degenerate parametric amplification in superconducting architectures have employed SQUIDs, which may be operated as charge-pumped or flux-pumped devices depending on how they are modulated. The most basic flux-pumped superconducting device consists of a single-loop dc SQUID [35, 48–50]. An external magnetic flux threads the SQUID loop and serves as the pump drive at frequency ω_p . This pump participates in a degenerate three-wave mixing process involving the signal and idler modes at frequencies ω_s and ω_i , respectively, satisfying $\omega_p = \omega_s + \omega_i \approx 2\omega_s$. When the bare cavity resonance is tuned near $\omega_a \approx \omega_s$, the flux modulation generates an effective two-photon drive. Operationally, this is achieved by biasing the SQUID at a static flux F and applying a small AC modulation such that the external flux takes the form $\Phi_e/\varphi_0 = F + \delta f \cos(\omega_p t)$, where δf is the modulation depth [14] and $\varphi_0 = h/2e$ is the flux quantum. A fundamental limitation of the single-loop SQUID design is that its Kerr nonlinearity cannot be mitigated [44, 51].

To enable Kerr cancellation, one must move beyond the minimal single-loop design. Multi-loop SQUID geometries introduce additional tunability that allows the leading-order nonlinearities to be engineered away. In such flux-pumped multi-loop SQUIDs, the static effective Hamiltonian expanded to fourth order in the zero-point phase fluctuations takes the general form [51]

$$\hat{H}_{\text{SQ}} = \hat{H}_{\text{DPA}} + K \hat{a}^{\dagger 2} \hat{a}^2 + \Lambda \left(\hat{a}^{\dagger 3} \hat{a} + \hat{a}^\dagger \hat{a}^3 \right) + \zeta \left(\hat{a}^{\dagger 4} + \hat{a}^4 \right), \quad (3)$$

where K is the Kerr nonlinearity, and Λ and ζ capture the other flux-dependent nonlinear corrections inherited from the underlying SQUID potential. A particularly useful realization is the symmetric two-loop SQUID (STS) circuit containing a linear inductor between the loops, as illustrated in Fig. 1. When both loops of STS are threaded by the same external flux modulation, $\Phi_{1e}/\varphi_0 = \Phi_{2e}/\varphi_0 = F + \delta f \cos(\omega_p t)$, the

Kerr coefficient becomes flux dependent and takes the form $K = -E_C \cos F/2$, where E_C is the charging energy of the circuit. Hence, the Kerr-coefficient vanishes at $F = -\pi/2$. At this same bias point, the quartic correction also cancels because $\zeta \propto \cos F$, leaving only the cubic nonlinear term (see the Supplemental Material for details). Consequently, the static effective Hamiltonian of the STS device simplifies to

$$\hat{H}_{\text{STS}} = \hat{H}_{\text{DPA}} + \Lambda \left(\hat{a}^\dagger \hat{a} + \hat{a}^\dagger \hat{a}^3 \right), \quad (4)$$

representing a substantial reduction in unwanted nonlinearities. However, since $\Lambda \propto \delta f \sin F$ (see Supplemental Material) takes a maximum at $F = \pi/2$, we will study in detail its impact on parametric amplification. It is important to note that a conventional single-loop SQUID cannot be biased at the symmetry point $F = -\pi/2$ because this corresponds to its “off” point where the Josephson energy is minimized and the resonance frequency approaches zero. As a result, single-loop flux-pumped JPA inevitably retains all nonlinear corrections in Eq. (3), including a nonzero Kerr nonlinearity, while the STS design permits systematic suppression of these terms. Throughout the remainder of this work, we refer to single-loop SQUID-based parametric amplifiers as JPA, and to double-loop STS-based devices as STS. The explicit expressions for K , Λ , and ζ for both circuit designs are provided in the Supplemental Material.

Nonidealities in JPA— Leading higher-order nonlinearities characterized by the coefficients K and Λ lead JPAs to deviate from ideal DPA dynamics, reducing their achievable squeezing and overall performance. This deviation is captured by comparing the JPA’s moments to those of an ideal DPA through the parameter [14]

$$\Xi_i = 1 - \frac{|M_i|}{\sqrt{N_i(N_i + 1/2)}}, \quad (5)$$

where $i \in \{\text{DPA, JPA}\}$, $M_i = \langle \hat{a}^2 \rangle - \langle \hat{a} \rangle^2$ and $N_i = \langle \hat{a}^\dagger \hat{a} \rangle - |\langle \hat{a} \rangle|^2$, $\Xi_{\text{DPA}} = 0$ and $\Xi_{\text{JPA}} \in [0, 1]$. By construction, $\Xi_{\text{JPA}} = 0$ corresponds to ideal DPA-level performance, while $\Xi_{\text{JPA}} \rightarrow 1$ indicates increasingly strong deviation from DPA behavior. Since we work in the weak-modulation regime ($\delta f \ll 1$) and the quartic term in \hat{H}_{SQ} scales as $\zeta \propto \delta f^2$ (whereas $K \propto \delta f^0$ and $\Lambda \propto \delta f^1$), we neglect the contribution from ζ in the remainder of this letter. To understand the limitations of single-loop SQUID JPAs and motivate the need for a double-loop STS architecture, we first examine the deviation parameter Ξ_{JPA} for various nonlinear contributions.

Figure 2(a) shows the deviation parameter Ξ_{JPA} , computed from the Hamiltonian in Eq. (3), as a function of the two-photon drive strength λ . We consider three scenarios: (i) both the Kerr and Λ nonlinearities present (black solid curve), (ii) only the Kerr nonlinearity included (orange dashed curve), and (iii) only the Λ correction retained as in the STS Hamiltonian (purple dot-dashed curve). Note that, The near-perfect overlap of the black and orange curves demonstrates that Λ has a negligible effect on Ξ_{JPA} over the parameter range studied, $|\lambda|/\kappa \in [0, 0.47]$. Note that, for $\Delta = 0$, the gain in

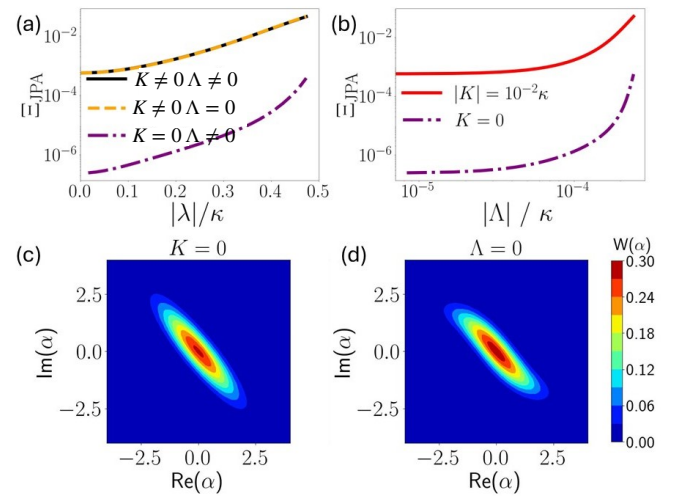


FIG. 2. (a) Deviation of JPAs from ideal DPA dynamics (Ξ_{JPA}) plotted as a function of drive strength λ . For $K \neq 0$, we consider $|K|/\kappa = 10^{-2}$ and $|\lambda|/\kappa \in [0, 0.47]$ corresponds to $|\Lambda|/\kappa \in [0, 2.36 \times 10^{-4}]$. (b) Deviation of JPAs plotted for $|K| = 10^{-2}\kappa$, and $K = 0$ as a function of Λ . Steady-state Wigner function plot for $|\lambda| = 0.45\kappa$ (indicated by stars in (a)) in the (c) Kerr-free case, $K = 0$, and (d) for $\Lambda = 0$. For (c), we consider $|\Lambda|/\kappa = 2.25 \times 10^{-4}$, whereas for (d), we consider $|K|/\kappa = 10^{-2}$. Note that, the $K = 0$ case can only be realized with an STS circuit. We take $\Delta = 0$ for all subfigures.

Eq. (2) diverges at $|\lambda_{\text{crit}}| = 0.5\kappa$. The upper bound on λ is chosen to ensure at least 25 dB of gain for the degenerate parametric amplifier (DPA). Since $\Lambda = (\Phi_{\text{zps}}/\varphi_0)^2 \lambda/6$ (see the Supplementary Material), where the zero point phase spread, $\Phi_{\text{zps}}/\varphi_0 \ll 1$, this corresponds to $|\Lambda|/\kappa \in [0, 2.36 \times 10^{-4}]$ for the case $\Lambda \neq 0$. By contrast, eliminating the Kerr nonlinearity, as realized in the STS Hamiltonian, leads to a substantial reduction in Ξ_{JPA} , bringing the system much closer to ideal DPA behavior. In Fig. 2(b), we examine Ξ_{JPA} as a function of Λ for different values of the Kerr coefficient. We find that Ξ_{JPA} is significantly larger in the presence of Kerr nonlinearity (red solid curve) than in its absence (purple dot-dashed curve), particularly in the weak two-photon driving regime. Nevertheless, even when $K = 0$, Ξ_{JPA} increases sharply for $\Lambda/\kappa \gtrsim 10^{-4}$ (as illustrated by the rise of purple dot-dashed curve). However, we will later show that deviations induced by Λ have a weaker effect on the amplifier gain and efficiency than those arising from Kerr nonlinearity. These observations are further corroborated by the Wigner-function plots in Fig. 2(c) and (d). Removing the Kerr term, as realized in the STS Hamiltonian, yields a nearly ideal squeezed state (Fig. 2(c)), whereas suppressing Λ alone while retaining Kerr results in strong state distortion (Fig. 2(d)). Thus, we conclude that the Kerr term in the Hamiltonian leads to stronger deviations than the cubic Λ term to the DPA Hamiltonian.

To further quantify how circuit nonidealities drive deviations from the DPA limit, we evaluate the squeezing level $S_f = \langle \Delta \hat{X}_{\text{vac}}^2 \rangle / \langle \Delta \hat{X}_{\text{min}}^2 \rangle$, where $\langle \Delta \hat{X}_{\text{vac}}^2 \rangle = 1/2$ is the vari-

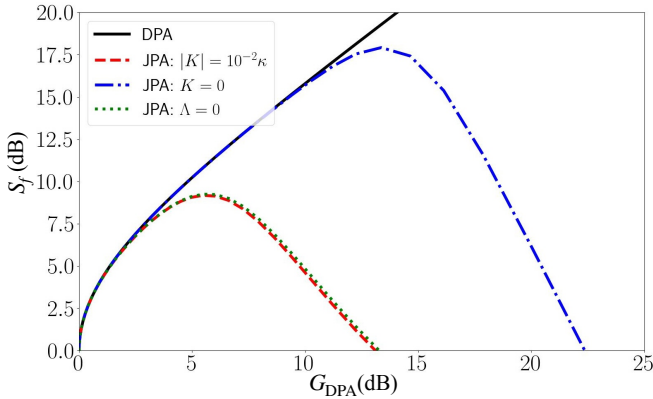


FIG. 3. Squeezing level for DPA, and JPAs plotted as a function of phase-preserving DPA gain. We consider, $\Delta = \gamma = 0$, $\kappa/2\pi = 300\text{MHz}$, Josephson inductance $L_J = 80\text{pH}$, and capacitance $C_\Sigma = 2\text{pF}$.

ance of the vacuum state and $\langle \Delta \hat{X}_{\min}^2 \rangle$ denotes the minimum variance of the output-field X quadrature [14, 52]. This metric provides a quantitative measure of how strongly each nonideality degrades squeezing. Figure 3 shows S_f as a function of DPA gain for four cases: an ideal DPA (black solid curve), a JPA including both nonidealities K and Λ (red dashed curve), a JPA with $K = 0$ as in the STS case (blue dot-dashed curve), and a JPA with $\Lambda = 0$ (green dotted curve). We observe that when both K and Λ are present, the squeezing level deviates markedly from the DPA benchmark beyond $\sim 5\text{dB}$ of gain, falling much below the ideal DPA squeezing. Eliminating Λ alone while retaining K (green dotted curve) yields nearly identical behavior, confirming that Kerr nonlinearity is the dominant source of squeezing degradation in this regime. In contrast, a Kerr-free JPA (blue dot-dashed curve) closely follows the DPA squeezing level up to approximately 15 dB of gain and exhibits a substantial improvement over the other configurations. Together, these results underscore the central role of Kerr nonlinearity in limiting the performance of single-SQUID JPAs and motivate the adoption of multi-loop circuit designs that enable systematic Kerr suppression.

Kerr-free STS parametric amplifier— The quantum Langevin equation for the STS parametric amplifier, as shown in Fig. (1), can be written as $\dot{\hat{a}} = i[\hat{H}_{\text{STS}}, \hat{a}] - \bar{\kappa}/2\hat{a} + \sqrt{\kappa}\hat{a}_{\text{in}} + \sqrt{\gamma}\hat{b}_{\text{in}}$, where \hat{a}_{in} and \hat{b}_{in} are the signal and undesired loss input fields, respectively. Since we compare the performance of the STS to a quantum-limited DPA ($\gamma = 0$), we assume a lossless cavity ($\gamma = 0$) for all amplifiers discussed in this letter (see Supplemental Material for analysis of the STS amplifier with $\gamma \neq 0$). The corresponding input–output relation is given by $\hat{a}_{\text{out}}(t) = \sqrt{\kappa}\hat{a}(t) - \hat{a}_{\text{in}}(t)$, which defines the output field carrying the amplified signal, \hat{a}_{out} .

Using semiclassical harmonic balance equations and input–output theory [23], the phase-preserving gain $G_{\text{STS}}(\omega)$ of the STS amplifier as a linear response to the signal probe at frequency ω_s can be expressed as (see the Supplemental Material

for harmonic balance and stability diagram analysis)

$$G_{\text{STS}}(\omega) = \left| \frac{i\kappa(\omega + \Delta_{\text{eff}}^* + i\frac{\kappa}{2})}{(\omega - \Delta_{\text{eff}} + i\frac{\kappa}{2})(\omega + \Delta_{\text{eff}}^* + i\frac{\kappa}{2}) + |\lambda_{\text{eff}}|^2} - 1 \right|^2. \quad (6)$$

Here, $\omega = \omega_s - \omega_p/2$ denotes the detuning of the signal from the rotating-frame frequency, while $\Delta_{\text{eff}} = \Delta + 3\Lambda\alpha_i\alpha_s$ and $\lambda_{\text{eff}} = \lambda + 9\Lambda n_s$ represent the effective detuning and two-photon drive strength, respectively. The mean intracavity field amplitudes at the signal and idler frequencies $\omega_{s,i}$ are denoted by $\alpha_{s,i}$, with the corresponding photon numbers given by $n_{s(i)} = |\alpha_{s(i)}|^2$. We find that the gain expression of the STS amplifier has the same functional form as that of an ideal DPA in Eq. (2), with the only difference being the presence of Λ -induced corrections to the effective detuning and drive strength. When the effective STS parameters are matched to those of the DPA ($\lambda_{\text{eff}} = \lambda_{\text{DPA}}$, $\Delta_{\text{eff}} = \Delta_{\text{DPA}}$), the STS amplifier exhibits the same gain–bandwidth performance as a quantum-limited DPA, as shown in the inset of Figure. 4(a).

Gain and efficiency in the linear response regime— We study the STS amplifier gain at the center frequency $\omega = \omega_s - \omega_p/2 = 0$. To compute the phase-preserving gain of the STS amplifier, we evaluate the cavity-field displacement induced by a narrow-band signal probe and the corresponding output response [14]. The probe is introduced via the Hamiltonian $\hat{H}_{\text{probe}} = \epsilon_{\text{probe}}\hat{a}^\dagger + \epsilon_{\text{probe}}^*\hat{a}$, where ϵ_{probe} is the probe amplitude. We operate in the linear-response regime by assuming a weak probe, $\epsilon_{\text{probe}} \ll \kappa$. Following Ref. [14], the input–output relation is then expressed in terms of the phase-sensitive gain matrix as [14]

$$\begin{bmatrix} \hat{X}_{\text{out}} \\ \hat{P}_{\text{out}} \end{bmatrix} = \begin{bmatrix} g_{11} & g_{12} \\ g_{21} & g_{22} \end{bmatrix} \begin{bmatrix} \hat{X}_{\text{in}} \\ \hat{P}_{\text{in}} \end{bmatrix}, \quad (7)$$

where the quadratures are defined as $\hat{X} = (\hat{a} + \hat{a}^\dagger)/\sqrt{2}$ and $\hat{P} = i(\hat{a}^\dagger - \hat{a})/\sqrt{2}$. The phase-preserving gain can then be expressed as [14], $G = |g_{11} + g_{22} + i(g_{21} - g_{12})|^2/4$.

We compute the gain by solving for the steady-state expectation values of the output quadratures with the input field amplitude, $\langle \hat{a}_{\text{in}} \rangle = i\epsilon_{\text{probe}}/\sqrt{\kappa}$. The steady state follows from the master equation [14], $\dot{\hat{a}} = -i[\hat{H}_{\text{STS}} + \hat{H}_{\text{probe}}, \hat{a}] + \kappa\mathcal{D}[\hat{a}]\hat{a}$, where $\mathcal{D}[\hat{a}]\hat{a} = \hat{a}\hat{a}^\dagger - (\hat{a}^\dagger\hat{a} + \hat{a}\hat{a}^\dagger)/2$ is the dissipation superoperator.

Figure 4(a) presents the phase-preserving gain of the STS amplifier alongside that of an ideal DPA and JPAs with varying Kerr nonlinearities. At low gain, the almost ideal JPA (red dot-dashed curve) closely follows the DPA response (solid black curve) and remains quantum-limited up to approximately 15 dB. At higher gain and stronger Kerr nonlinearity, however, the JPA gain falls below the DPA value for the same drive strength λ , indicating that increasing Kerr nonlinearity restricts the range of quantum-limited operation (compare the dot-dashed red curve with dotted blue and dashed green curves). In contrast, the Kerr-free STS amplifier (dashed orange curve) remains quantum-limited up to 25 dB of gain, demonstrating that the residual nonideality Λ is too weak to appreciably degrade its performance.

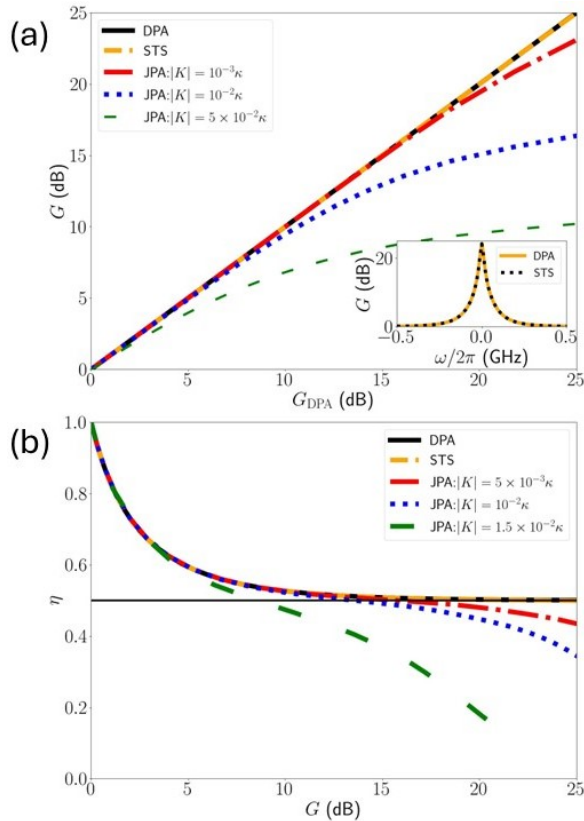


FIG. 4. (a) Phase-preserving gain plotted against DPA gain and (b) Phase-preserving quantum efficiency plotted at $\omega = 0$ against the given design's gain for DPA, Kerr-free STS amplifier, and single-SQUID JPAs with varying Kerr nonlinearities. Inset in (a) shows the phase-preserving gain calculated using Eq. (6) against signal detuning ω for DPA and STS amplifier. We take $\Delta = \gamma = 0$, $\kappa/2\pi = 300\text{MHz}$, and the sweep for the two-photon drive $0 \leq \lambda < \kappa/2$. For STS, we consider capacitance $C_\Sigma = 4\text{pF}$, Josephson inductance $L_J = 80\text{pH}$, and linear inductance $L = 100\text{pH}$.

The phase-preserving quantum efficiency provides a direct measure of an amplifier's proximity to quantum-limited operation. For a linear quantum amplifier, the ideal efficiency is given by [14, 53, 54]

$$\eta = (1 + 2\mathcal{A})^{-1}, \quad (8)$$

where the added noise number $\mathcal{A} = \langle |\Delta\hat{a}_{\text{in}}|^2 \rangle / G$ characterizes the mean-square fluctuation of the input signal normalized by the gain [53]. The fluctuation is defined as $\langle |\Delta\hat{a}|^2 \rangle = \langle |\hat{a}, \hat{a}^\dagger| \rangle / 2 - |\langle \hat{a} \rangle|^2$. The added noise is fundamentally constrained by the Heisenberg uncertainty principle [15, 16, 53], with a lower bound $\mathcal{A} \geq (G - 1)/(2G)$, corresponding to half a photon of noise in the high-gain limit.

As shown in Fig. 4(b), the DPA (solid black curve) exhibits unit efficiency at zero gain, reflecting the absence of added noise, and converges to an efficiency of 0.5 at gains exceeding 15dB. JPAs with finite Kerr nonlinearity coincide with the DPA in the low-gain regime but require increased added noise to reach higher gains, leading to efficiencies below the quan-

tum limit. This degradation becomes more pronounced with increasing Kerr nonlinearity. In contrast, the Kerr-free STS amplifier (orange dashed curve) remains overlapped with the DPA even in the high-gain regime despite the presence of the Λ term. Together, the gain and efficiency results demonstrate that the residual nonideality Λ in the STS Hamiltonian is practically negligible over the gain range considered.

We find that the dip appearing in the squeezing level S_f at high gain does not manifest in the gain and efficiency, since these quantities probe different aspects of the output field and exhibit distinct sensitivities to the Λ contribution (compare the blue dot-dashed curve in Fig. 3 and orange dashed curves in Fig. 4 (a) and (b)). The squeezing level depends exclusively on the variance of the squeezed \hat{X} quadrature and is therefore highly sensitive to the off-diagonal gain element that arises from quadrature mixing and non-Gaussian distortions. At high gain, where the diagonal element associated with squeezing becomes small, even weak Λ can significantly enhance these off-diagonal contributions, leading to a reduction in S_f . By contrast, the phase-preserving gain and efficiency are governed primarily by the amplification of the anti-squeezed \hat{P} quadrature at high gain, which remains the dominant contribution even in the presence of Λ , thereby mitigating the influence of off-diagonal gain elements to a larger extent. In addition to gain and efficiency performances, we also characterize the stability diagram for the STS amplifier in the space of parameters Δ and λ (see the Supplemental Material). We see that at $G = 25$ dB ($\Delta = 0$, $|\lambda|/\kappa \approx 0.47$), the STS amplifier is in bi-stable region with two stable points. However, since the two stable points are separated by a distance beyond the intracavity population of the amplifier, STS is effectively in a mono-stable region with a trivial ground state, just like a DPA.

In conclusion, using the deviation parameter Ξ_{JPA} , intracavity Wigner-function plots, and squeezing level, we have demonstrated that Kerr nonlinearity is the dominant nonideality in single-SQUID JPAs and is primarily responsible for their departure from ideal DPA behavior. We further showed that our flux-pumped STS architecture enables systematic cancellation of the Kerr nonlinearity by operating at a static flux bias $F = -\pi/2$, a regime inaccessible to single-loop SQUID JPAs. Through both analytical expressions and numerical simulations of phase-preserving gain and efficiency, we established that the STS amplifier closely emulates ideal DPA performance and substantially outperforms single-loop SQUID JPAs up to gains of 25 dB. The resulting enhancements in squeezing, gain, and efficiency open new opportunities for high-fidelity superconducting qubit readout and quantum feedback applications [55, 56].

ACKNOWLEDGEMENTS

We acknowledge helpful discussions with Kevin P. O'Brien. This work was supported by the Army Research Office through Grant No. W911NF22-1-0258.

* Correspondence should be addressed to: bbhanderi@chapman.edu

[1] A. Wallraff, D. I. Schuster, A. Blais, L. Frunzio, R.- S. Huang, J. Majer, S. Kumar, S. M. Girvin, and R. J. Schoelkopf, Strong coupling of a single photon to a superconducting qubit using circuit quantum electrodynamics, *Nature (London)* **431**, 162 (2004).

[2] C. Gaikwad, D. Kowsari, W. Chen, and K. W. Murch, Observing parity-time symmetry breaking in a Josephson parametric amplifier, *Phys. Rev. Res.* **5**, L042024 (2023).

[3] Y. Lu, M. Kudra, T. Hillmann, J. Yang, H.-X. Li, F. Quijandría, and P. Delsing, Resolving Fock states near the Kerr-free point of a superconducting resonator, *npj Quantum Inf.* **9**, 114 (2023).

[4] A. Dorogov, G. Fedorov, D. Kalacheva, A. Dmitriev, A. Bolgar, N. Abramov, and O. Astafiev, Application of a broadband Josephson parametric amplifier, *St Petersburg Polytechnical University Journal Physics and Mathematics* **15** (2022).

[5] S. Schaal, I. Ahmed, J. A. Haigh, L. Hutin, B. Bertrand, S. Barraud, M. Vinet, C.-M. Lee, N. Stelmashenko, J. W. A. Robinson, and et al., Fast gate-based readout of silicon quantum dots using Josephson parametric amplification, *Phys. Rev. Lett.* **124**, 067701 (2020).

[6] S. Shankar, Z. Hao, M. Hatipour, W. Strickland, T. Shaw, and J. Shabani, Josephson parametric amplifiers for rapid, high-fidelity measurement of solid-state qubits, in *2023 Device Research Conference (DRC)* (IEEE, Santa Barbara, 2023) p. 1.

[7] T. White, A. Opremcak, G. Sterling, A. Korotkov, D. Sank, R. Acharya, M. Ansmann, F. Arute, K. Arya, J. C. Bardin, and et al., Readout of a quantum processor with high dynamic range Josephson parametric amplifiers, *Appl. Phys. Lett.* **122**, 014001 (2023).

[8] M. H. Devoret and R. J. Schoelkopf, Superconducting circuits for quantum information: an outlook, *Science* **339**, 1169 (2013).

[9] H.-L. Huang, D. Wu, D. Fan, and X. Zhu, Superconducting quantum computing: a review, *Science China Information Sciences* **63**, 180501 (2020).

[10] L. B. Nguyen, Y. Kim, A. Hashim, N. Goss, B. Marinelli, B. Bhandari, D. Das, R. K. Naik, J. M. Kreikebaum, A. N. Jordan, and et al., Programmable Heisenberg interactions between Floquet qubits, *Nat. Phys.* **20**, 240 (2024).

[11] P. Krantz, A. Bengtsson, M. Simoen, S. Gustavsson, V. Shumeiko, W. D. Oliver, C. M. Wilson, P. Delsing, and J. Bylander, Single-shot read-out of a superconducting qubit using a Josephson parametric oscillator, *Nat. Commun.* **7**, 11417 (2016).

[12] J. Aumentado, Prospects for parametric amplifiers in large-scale superconducting quantum computing, in *2022 IEEE/MTT-S International Microwave Symposium - IMS 2022* (IEEE, Denver, 2022) p. 76.

[13] J. Aumentado, Superconducting parametric amplifiers: The state of the art in Josephson parametric amplifiers, *IEEE Microwave Magazine* **21**, 45 (2020).

[14] S. Boutin, D. M. Toyli, A. V. Venkatramani, A. W. Eddins, I. Siddiqi, and A. Blais, Effect of higher-order nonlinearities on amplification and squeezing in Josephson parametric amplifiers, *Phys. Rev. Appl.* **8**, 054030 (2017).

[15] C. M. Caves, Quantum-mechanical noise in an interferometer, *Phys. Rev. D* **23**, 1693 (1981).

[16] C. M. Caves, Quantum limits on noise in linear amplifiers, *Phys. Rev. D* **26**, 1817 (1982).

[17] A. N. Jordan and I. A. Siddiqi, *Quantum Measurement: Theory and Practice* (Cambridge University Press, 2024).

[18] D. Walls and G. J. Milburn, Quantum information, in *Quantum optics*, edited by G. J. Milburn (Springer, 2008) pp. 307–346.

[19] M. O. Scully and M. S. Zubairy, *Quantum Optics* (Cambridge University Press, 1997).

[20] G. Liu, A. Lingenfelter, V. Joshi, N. Frattini, V. Sivak, S. Shankar, and M. Devoret, Fully directional quantum-limited phase-preserving amplifier, *Phys. Rev. Appl.* **21**, 014021 (2024).

[21] N. Bergeal, F. Schackert, M. Metcalfe, R. Vijay, V. E. Manucharyan, L. Frunzio, D. E. Prober, R. J. Schoelkopf, S. M. Girvin, and M. H. Devoret, Phase-preserving amplification near the quantum limit with a Josephson ring modulator, *Nature (London)* **465**, 64 (2010).

[22] A. Roy and M. Devoret, Quantum-limited parametric amplification with Josephson circuits in the regime of pump depletion, *Phys. Rev. B* **98**, 045405 (2018).

[23] N. E. Frattini, V. V. Sivak, A. Lingenfelter, S. Shankar, and M. H. Devoret, Optimizing the nonlinearity and dissipation of a SNAIL parametric amplifier for dynamic range, *Phys. Rev. Appl.* **10**, 054020 (2018).

[24] M. Malnou, D. A. Palken, L. R. Vale, G. C. Hilton, and K. W. Lehnert, Optimal operation of a Josephson parametric amplifier for vacuum squeezing, *Phys. Rev. Appl.* **9**, 044023 (2018).

[25] C. Gaikwad, D. Kowsari, W. Chen, and K. W. Murch, Observing parity-time symmetry breaking in a Josephson parametric amplifier, *Phys. Rev. Res.* **5**, L042024 (2023).

[26] B. Qing, L. B. Nguyen, X. Liu, H. Ren, W. P. Livingston, N. Goss, A. Hajr, T. Chistolini, Z. Pedramrazi, D. I. Santiago, J. Luo, and I. Siddiqi, Broadband coplanar-waveguide-based impedance-transformed Josephson parametric amplifier, *Phys. Rev. Res.* **6**, L012035 (2024).

[27] T.-C. Chien, O. Lanes, C. Liu, X. Cao, P. Lu, S. Motz, G. Liu, D. Pekker, and M. Hatridge, Multiparametric amplification and qubit measurement with a Kerr-free Josephson ring modulator, *Phys. Rev. A* **101**, 042336 (2020).

[28] R. Vijay, D. H. Slichter, and I. Siddiqi, Observation of quantum jumps in a superconducting artificial atom, *Phys. Rev. Lett.* **106**, 110502 (2011).

[29] W. Dai, G. Liu, V. Joshi, A. Miano, V. Sivak, S. Shankar, and M. H. Devoret, Optimizing the pump coupling for a three-wave-mixing Josephson parametric amplifier, *Phys. Rev. Appl.* **23**, 054069 (2025).

[30] J. Grebel, A. Bienfait, E. Dumur, H. Chang, M. Chou, C. R. Conner, G. A. Peairs, R. G. Povey, Y. P. Zhong, and A. N. Cleland, Flux-pumped impedance-engineered broadband Josephson parametric amplifier, *Appl. Phys. Lett.* **118**, 142601 (2021).

[31] T. Roy, S. Kundu, M. Chand, A. M. Vadiraj, A. Ranadive, N. Nehra, M. P. Patankar, J. Aumentado, A. A. Clerk, and R. Vijay, Broadband parametric amplification with impedance engineering: Beyond the gain-bandwidth product, *Appl. Phys. Lett.* **107**, 262601 (2015).

[32] K. He, G. Dai, Q. Yu, Y. He, C. Zhao, J. Liu, and W. Chen, Simulation of a flux-pumped Josephson parametric amplifier with a detailed SQUID model using the harmonic balance method, *Superconductor Science and Technology* **36**, 045010 (2023).

[33] A. Kamal, A. Marblestone, and M. Devoret, Signal-to-pump back action and self-oscillation in double-pump Josephson parametric amplifier, *Phys. Rev. B* **79**, 184301 (2009).

[34] C. Eichler, Ph.D. thesis, ETH Zurich (2013).

[35] T. Yamamoto, K. Inomata, M. Watanabe, K. Matsuba, T. Miyazaki, W. D. Oliver, Y. Nakamura, and J. S. Tsai, Flux-driven Josephson parametric amplifier, *Appl. Phys. Lett.* **93**, 042510 (2008).

[36] Y. Xu, Z. Hua, W. Wang, Y. Ma, M. Li, J. Chen, J. Zhou, X. Pan, L. Xiao, H. Huang, W. Cai, H. Ai, Y.-x. Liu, C.-L. Zou,

and L. Sun, Dynamic compensation for pump-induced frequency shift in kerr-cat qubit initialization, *Phys. Rev. Appl.* **23**, 034060 (2025).

[37] J. Y. Mutus, T. C. White, R. Barends, Y. Chen, Z. Chen, B. Chiaro, A. Dunsworth, E. Jeffrey, J. Kelly, A. Megrant, *et al.*, Strong environmental coupling in a Josephson parametric amplifier, *Appl. Phys. Lett.* **104** (2014).

[38] B. A. Kochetov and A. Fedorov, Higher-order nonlinear effects in a Josephson parametric amplifier, *Phys. Rev. B* **92**, 224304 (2015).

[39] G. Liu, T.-C. Chien, X. Cao, O. Lanes, E. Alpern, D. Pekker, and M. Hatridge, Josephson parametric converter saturation and higher order effects, *Appl. Phys. Lett.* **111**, 202603 (2017).

[40] V. Sivak, N. Frattini, V. Joshi, A. Lingenfelter, S. Shankar, and M. Devoret, Kerr-free three-wave mixing in superconducting quantum circuits, *Phys. Rev. Appl.* **11**, 054060 (2019).

[41] A. Miano, G. Liu, V. V. Sivak, N. E. Frattini, V. R. Joshi, W. Dai, L. Frunzio, and M. H. Devoret, Frequency-tunable Kerr-free three-wave mixing with a gradiometric SNAIL, *Appl. Phys. Lett.* **120**, 184002 (2022).

[42] A. Haja, B. Qing, K. Wang, G. Koolstra, Z. Pedramrazi, Z. Kang, L. Chen, L. B. Nguyen, C. Jünger, N. Goss, and et al., High-coherence Kerr-cat qubit in 2D architecture, *Phys. Rev. X* **14**, 041049 (2024).

[43] B. Qing, A. Haja, K. Wang, G. Koolstra, L. B. Nguyen, J. Hines, I. Huang, B. Bhandari, Z. Padramrazi, L. Chen, and et al., Kerr-cat qubit operations below the fault-tolerant threshold, [arXiv:2411.04442](https://arxiv.org/abs/2411.04442) (2024).

[44] B. Bhandari, I. Huang, A. Haja, K. Yanik, B. Qing, K. Wang, D. I. Santiago, J. Dressel, I. Siddiqi, and A. N. Jordan, Symmetrically threaded superconducting quantum interference devices as next-generation Kerr-cat qubits, *PRX Quantum* **6**, 030338 (2025).

[45] A. Maiti, J. W. Garmon, Y. Lu, A. Miano, L. Frunzio, and R. J. Schoelkopf, Linear quantum coupler for clean bosonic control, *PRX Quantum* **6**, 040326 (2025).

[46] W. Wustmann and V. Shumeiko, Parametric resonance in tunable superconducting cavities, *Phys. Rev. B* **87**, 184501 (2013).

[47] C. Laflamme and A. A. Clerk, Quantum-limited amplification with a nonlinear cavity detector, *Phys. Rev. A* **83**, 033803 (2011).

[48] A. Zorin, Flux-driven Josephson traveling-wave parametric amplifier, *Phys. Rev. Appl.* **12**, 044051 (2019).

[49] L. Planat, R. Dassonneville, J. P. Martínez, F. Foroughi, O. Buisson, W. Hasch-Guichard, C. Naud, R. Vijay, K. Murch, and N. Roch, Understanding the saturation power of Josephson parametric amplifiers made from SQUID arrays, *Phys. Rev. Appl.* **11**, 034014 (2019).

[50] M. Hatridge, R. Vijay, D. H. Slichter, J. Clarke, and I. Siddiqi, Dispersive magnetometry with a quantum limited SQUID parametric amplifier, *Phys. Rev. B* **83**, 134501 (2011).

[51] Z. Hua, Y. Xu, W. Wang, Y. Ma, J. Zhou, W. Cai, H. Ai, Y.-x. Liu, M. Li, C.-L. Zou, and L. Sun, Engineering the nonlinearity of bosonic modes with a multiloop SQUID, *Phys. Rev. Appl.* **23**, 054031 (2025).

[52] L. Zhong, E. P. Menzel, R. Di Candia, P. Eder, M. Ihmig, A. Baust, M. Haeberlein, E. Hoffmann, K. Inomata, T. Yamamoto, and et al., Squeezing with a flux-driven Josephson parametric amplifier, *New J. Phys.* **15**, 125013 (2013).

[53] C. M. Caves, J. Combes, Z. Jiang, and S. Pandey, Quantum limits on phase-preserving linear amplifiers, *Phys. Rev. A* **86**, 063802 (2012).

[54] K. Peng, M. Naghiloo, J. Wang, G. D. Cunningham, Y. Ye, and K. P. O'Brien, Floquet-mode traveling-wave parametric amplifiers, *PRX Quantum* **3**, 020306 (2022).

[55] K. W. Murch, S. Weber, C. Macklin, and I. Siddiqi, Observing single quantum trajectories of a superconducting quantum bit, *Nature (London)* **502**, 211 (2013).

[56] R. Vijay, C. Macklin, D. Slichter, S. Weber, K. Murch, R. Naik, A. N. Korotkov, and I. Siddiqi, Stabilizing Rabi oscillations in a superconducting qubit using quantum feedback, *Nature (London)* **490**, 77 (2012).

Supplemental Material for “Flux Pumped Kerr-Free Parametric Amplifier”

FLUX-PUMPED JOSEPHSON PARAMETRIC AMPLIFIERS: CIRCUIT QUANTUM ELECTRODYNAMICS

In this section, we will study the circuit quantization in the presence of time-dependent flux for a DC SQUID, STS with an inductor in the middle branch as shown in Fig. 6, and STS with a Josephson junction in the middle branch [1]. We will show how the STS design with an inductor in the middle branch cancels the Kerr-nonlinearity through proper tuning of the external flux through the SQUID loops. We will also show that a Kerr-free operational point cannot be realized with the other designs considered.

DC SQUID

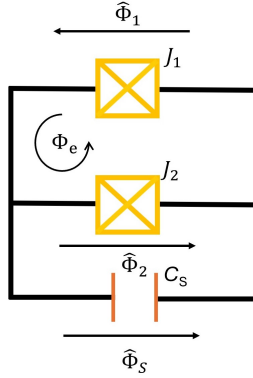


FIG. 5. Circuit design of the flux-pumped JPA. The junctions J_1 and J_2 compose the DC SQUID, which is shunted by capacitance C_S . The loop between J_1 and J_2 is threaded by an external flux Φ_e . $\hat{\Phi}_{1,2,S}$ are the branch flux operators.

We consider a flux-pumped Josephson parametric amplifier (JPA) [2], consisting of a DC SQUID driven by an external magnetic flux Φ_e , as illustrated in Fig. 5. The time-dependent external flux serves as the pumping mechanism essential for the operation of the parametric amplifier.

Following Ref. [3], the Hamiltonian for a parametrically driven DC SQUID in the lab frame can be written as

$$\hat{H}_{\text{lab},\text{JPA}} = 4E_C\hat{n}^2 - E_{J1}\cos\left(\frac{\hat{\Phi} - \Phi_e/2}{\varphi_0}\right) - E_{J2}\cos\left(\frac{\hat{\Phi} + \Phi_e/2}{\varphi_0}\right), \quad (\text{S1})$$

where $\varphi_0 = \hbar/2e$ is the reduced flux quantum, and the reduced charge operator $\hat{n} = in_0(\hat{a}^\dagger - \hat{a})$ and flux operator $\hat{\Phi} = \Phi_{\text{zps}}(\hat{a}^\dagger + \hat{a})$ are expressed in terms of the bosonic creation (\hat{a}^\dagger) and annihilation operators (\hat{a}). Further, $\Phi_{\text{zps}} = 2\varphi_0\sqrt{E_C/\omega_a}$ is the zero point flux fluctuations where ω_a is the bare resonator frequency. The external flux, $\Phi_e/2\varphi_0 = F + \delta f \cos(\omega_p t)$, where F is the static flux, $\omega_p \approx 2\omega_a$ is the pump frequency and δf is the pump modulation depth. E_{J1} and E_{J2} are the junction energies while C_1 and C_2 are the capacitances of junctions J_1 and J_2 . The DC SQUID is shunted by capacitance C_S . The charging energy is defined as $E_C = e^2/2C_\Sigma$ with $C_\Sigma = C_1 + C_2 + C_S$. While deriving Eq. (S1), we considered $C_1 = C_2$. Assuming symmetric Josephson junctions, $E_{J1} = E_{J2} = E_J$, the Hamiltonian reduces to

$$\hat{H}_{\text{lab},\text{JPA}} = 4E_C\hat{n}^2 - 2E_J\cos\left(\frac{\Phi_e}{2\varphi_0}\right)\cos\left(\frac{\hat{\Phi}}{\varphi_0}\right). \quad (\text{S2})$$

Following the methods in Ref. [2], we expand the JPA Hamiltonian up to fourth order in Φ_{zps} and assume weak modulation depth, $\delta f \approx (\Phi_{\text{zps}}/\varphi_0)$. Then evaluating the Hamiltonian in rotating frame at frequency $\omega_p/2$ and applying rotating wave approximation (RWA), we obtain [2]

$$\hat{H}_{\text{JPA}} = \Delta_f\hat{a}^\dagger\hat{a} + \frac{\lambda_f}{2}(\hat{a}^{\dagger 2} + \hat{a}^2) + K_f\hat{a}^{\dagger 2}\hat{a}^2 + \Lambda_f(\hat{a}^\dagger\hat{a}^3 + \hat{a}^{\dagger 3}\hat{a}) + \zeta_f(\hat{a}^{\dagger 4} + \hat{a}^4), \quad (\text{S3})$$

where $\Delta_f = \omega_a - \omega_p/2 + 2K_f$ is the effective detuning, $\lambda_f = E_J^{(1)}(\Phi_{zps}/\varphi_0)^2/2$ is the effective pump strength, $K_f = -E_J^{(0)}(\Phi_{zps}/\varphi_0)^4/4$ is the Kerr nonlinearity, and $\Lambda_f = -E_J^{(1)}(\Phi_{zps}/\varphi_0)^4/12$ and $\zeta_f = -E_J^{(2)}(\Phi_{zps}/\varphi_0)^4/48$ are the extra nonidealities. $E_J^{(0)}, E_J^{(2)} \propto \cos F$, and $E_J^{(1)} \propto \sin F$ [2]. Given that Kerr is the leading nonideality that needs to be cancelled to approach quantum-limited amplification [2], we need to operate SQUID at static flux $F = -\pi/2$. However, at $\Phi_e/2\varphi_0 = \pi/2$, $\hat{H}_{\text{lab},\text{JPA}} = 4E_C\hat{n}^2$, and the SQUID reduces to a capacitor. Hence, the SQUID cannot be operated around $F = \pi/2$ where the Kerr nonlinearity vanishes.

STS Design with an Inductor

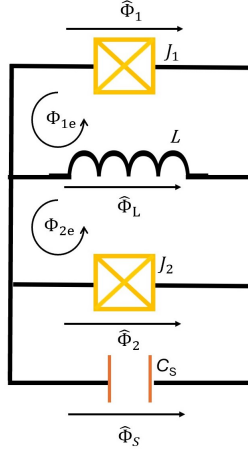


FIG. 6. STS circuit with an inductor in the middle branch: The outer branches are composed of junctions J_1 and J_2 whereas the middle branch consists of an inductor L . The double SQUID loop ($J_1 - L - J_2$) is shunted by a capacitor C_S . The loop between $J_{1(2)}$ and L is threaded by an external flux $\Phi_{1(2)e}$. $\hat{\Phi}_j$, where $j = 1, 2, L, S$, are the branch flux operators.

In search for a circuit design that can provide a Kerr-free amplifier, we propose a symmetrically threaded SQUID (STS) design discussed in Ref. [1]. However, in this STS design, we replaced the Josephson junction in the middle branch with a linear inductor with inductance L , as shown in Fig. 6. The bottom branch contains a Josephson junction J_2 shunted by capacitance C_2 whereas the top branch has a junction J_1 and capacitance C_1 . The circuit is shunted by a capacitance C_S . Similar to the case of DC SQUID, we start the circuit quantization by expressing the Lagrangian in terms of the branch flux operators. We obtain

$$\hat{\mathcal{L}} = \frac{1}{2}C_S\dot{\hat{\Phi}}_S^2 + \frac{1}{2}C_1\dot{\hat{\Phi}}_1^2 + \frac{1}{2}C_2\dot{\hat{\Phi}}_2^2 + \frac{1}{2}C_L\dot{\hat{\Phi}}_L^2 + E_{J1}\cos\left(\frac{\hat{\Phi}_1}{\varphi_0}\right) + E_{J2}\cos\left(\frac{\hat{\Phi}_2}{\varphi_0}\right) - \frac{1}{2}E_L\left(\frac{\hat{\Phi}_L}{\varphi_0}\right)^2, \quad (\text{S4})$$

where $\varphi_0 = \hbar/2e$ is the reduced flux quantum, $E_L = \varphi_0^2/L$, and $\hat{\Phi}_{1,2,L,S}$ are the branch flux operators. We have the following constraints due to flux quantization in the two SQUID loops, $\hat{\Phi}_L - \hat{\Phi}_1 = \Phi_{1e}$ and $\hat{\Phi}_2 - \hat{\Phi}_L = \Phi_{2e}$. Hence, the branch flux operators $\hat{\Phi}_1$, $\hat{\Phi}_2$, and $\hat{\Phi}_L$ are not independent. Since the sum of all capacitances in parallel gives the total capacitance, we can assume that the shunting capacitance C_S is distributed equally to junctions J_1 and J_2 as additional capacitance to $C_{1,2}$. Then, using Kirchoff's voltage law, the Lagrangian can be rewritten as

$$\hat{\mathcal{L}} = \frac{1}{2}\left(C_1 + \frac{C_S}{2}\right)\dot{\hat{\Phi}}_1^2 + \frac{1}{2}\left(C_2 + \frac{C_S}{2}\right)\dot{\hat{\Phi}}_2^2 + \frac{1}{2}C_L\dot{\hat{\Phi}}_L^2 + E_{J1}\cos\left(\frac{\hat{\Phi}_1}{\varphi_0}\right) + E_{J2}\cos\left(\frac{\hat{\Phi}_2}{\varphi_0}\right) - \frac{1}{2}E_L\left(\frac{\hat{\Phi}_L}{\varphi_0}\right)^2, \quad (\text{S5})$$

Following Ref. [3], given that the circuit loops threaded by time-dependent fluxes have three branches and two meshes, we have a single degree of freedom in the circuit. We pick this free variable as $\tilde{\Phi}$ to govern the dynamics between the branch fluxes that are constrained by external flux loops Φ_{1e} and Φ_{2e} , defined through $\tilde{\Phi} = m_L\hat{\Phi}_L + m_1\hat{\Phi}_1 + m_2\hat{\Phi}_2$ where m_L , m_1 , and m_2 are weights that allocate the external flux to the different branches. Then we can solve for branch flux operators $\hat{\Phi}_L$, $\hat{\Phi}_1$, and $\hat{\Phi}_2$ in

terms of $\tilde{\hat{\Phi}}$, Φ_{1e} , and Φ_{2e} , and obtain

$$\hat{\Phi}_L = \frac{1}{m_\Sigma} \left[\tilde{\hat{\Phi}} + m_1 \Phi_{1e} - m_2 \Phi_{2e} \right], \quad (S6)$$

$$\hat{\Phi}_1 = \frac{1}{m_\Sigma} \left[\tilde{\hat{\Phi}} - (m_2 + m_L) \Phi_{1e} - m_2 \Phi_{2e} \right], \quad (S7)$$

$$\hat{\Phi}_2 = \frac{1}{m_\Sigma} \left[\tilde{\hat{\Phi}} + m_1 \Phi_{1e} + (m_1 + m_L) \Phi_{2e} \right], \quad (S8)$$

where $m_\Sigma = m_1 + m_2 + m_L$. Substituting the above expressions into the Lagrangian, applying Legendre transformation, and neglecting the terms $\propto \dot{\hat{\Phi}}_{1e}^2, \dot{\hat{\Phi}}_{2e}^2, \dot{\Phi}_{1e} \dot{\Phi}_{2e}$, we obtain

$$\begin{aligned} \hat{\mathcal{L}} = 4E_C \dot{n}^2 + \frac{\dot{\tilde{\hat{\Phi}}}}{m_\Sigma^2} \left\{ \left[\left(C_2 + \frac{C_S}{2} + C_L \right) m_1 - \left(C_1 + \frac{C_S}{2} \right) m_2 - \left(C_1 + \frac{C_S}{2} \right) m_L \right] \dot{\Phi}_{1e} \right. \\ \left. + \left[\left(C_2 + \frac{C_S}{2} \right) m_1 - \left(C_1 + \frac{C_S}{2} + C_L \right) m_2 + \left(C_2 + \frac{C_S}{2} \right) m_L \right] \dot{\Phi}_{2e} \right\} + E_{J1} \cos \left(\frac{\hat{\Phi}_1}{\varphi_0} \right) + E_{J2} \cos \left(\frac{\hat{\Phi}_2}{\varphi_0} \right) - \frac{1}{2} E_L \left(\frac{\hat{\Phi}_L}{\varphi_0} \right)^2, \end{aligned} \quad (S9)$$

where the reduced charge operator $\hat{n} = in_0(\hat{a}^\dagger - \hat{a})$ and flux operator $\tilde{\hat{\Phi}} = \Phi_{zps}(\hat{a}^\dagger + \hat{a})$ are expressed in terms of the bosonic creation (\hat{a}^\dagger) and annihilation operators (\hat{a}), and Φ_{zps} is the zero point flux fluctuations. Moreover, $E_C = e^2/2C_\Sigma$, where $C_\Sigma = C_1 + C_2 + C_L + C_S$. There are terms that mix $\tilde{\hat{\Phi}}$ with the external fluxes which can be eliminated by choosing m_L , m_1 , and m_2 such that the second term on the right hand side of Eq. (S9) is 0. This gives us the conditions $(C_2 + C_S/2 + C_L)m_1 - (C_1 + C_S/2)m_2 - (C_1 + C_S/2)m_L = 0$ and $(C_2 + C_S/2)m_1 - (C_1 + C_S/2 + C_L)m_2 - (C_2 + C_S/2)m_L = 0$. Since we have 2 equations and 3 unknowns, we have one degree of freedom. Using m_2 as the free variable, the solutions to the set of equations above are $m_L = m_2 C_L / (C_2 + C_S/2)$, $m_1 = m_2 (C_1 + C_S/2) / (C_2 + C_S/2)$, $m_2 = m_2$, and $m_\Sigma = m_2 C_\Sigma / (C_2 + C_S/2)$. We can simplify further by setting $m_2 = (C_2 + C_S/2)/C_\Sigma$ since it is the free variable, and it allows us to make the previous arbitrary choice of $m_\Sigma = 1$. Furthermore, considering $C_L = 0$, assuming symmetric junctions where $E_{J2} = E_{J1} = E_J$, and using the trigonometric identity $\cos A + \cos B = 2 \cos((A+B)/2) \cos((A-B)/2)$, we obtain

$$\begin{aligned} \hat{\mathcal{L}} = 4E_C \dot{n}^2 + \frac{1}{2} E_L \left(\frac{\tilde{\hat{\Phi}}}{\varphi_0} - \frac{C_2 + C_S/2}{C_\Sigma} \frac{\Phi_{2e}}{\varphi_0} + \frac{C_1 + C_S/2}{C_\Sigma} \frac{\Phi_{1e}}{\varphi_0} \right)^2 \\ + 2E_J \cos \left(\frac{\Phi_{1e} + \Phi_{2e}}{2\varphi_0} \right) \cos \left(\frac{\tilde{\hat{\Phi}}}{\varphi_0} + \frac{C_1 - C_2}{2C_\Sigma} \frac{\Phi_{1e} + \Phi_{2e}}{\varphi_0} \right). \end{aligned} \quad (S10)$$

We take $C_1 = C_2$. Then we can define the Hamiltonian in the lab frame as

$$\hat{H}_{\text{lab}} = 4E_C \dot{n}^2 + \frac{1}{2} E_L \left(\frac{\tilde{\hat{\Phi}} + \Phi_\Delta}{\varphi_0} \right)^2 - 2E_J \cos \left(\frac{\Phi_\Sigma}{\varphi_0} \right) \cos \left(\frac{\tilde{\hat{\Phi}}}{\varphi_0} \right), \quad (S11)$$

where $\Phi_\Delta = (\Phi_{1e} - \Phi_{2e})/2$ and $\Phi_\Sigma = (\Phi_{1e} + \Phi_{2e})/2$. For STS design, $\Phi_{1e} = \Phi_{2e} = \Phi_e$, and $\Phi_\Delta = 0$ so that we can express the Hamiltonian as

$$\hat{H}_{\text{lab}} = 4E_C \dot{n}^2 + \frac{1}{2} E_L \left(\frac{\tilde{\hat{\Phi}}}{\varphi_0} \right)^2 - 2E_J \cos \left(\frac{\Phi_e}{\varphi_0} \right) \cos \left(\frac{\tilde{\hat{\Phi}}}{\varphi_0} \right), \quad (S12)$$

where the external flux $\Phi_e/\varphi_0 = F + \delta f \cos(\omega_p t)$ depends on the static flux F and oscillating pump flux. Using our previous definitions for the reduced charge and flux operators in terms of bosonic operators, and expanding the cosine potential, we obtain

$$\hat{H}_{\text{lab}} = -4E_C n_0^2 (\hat{a}^\dagger - \hat{a})^2 + \frac{1}{2} E_L \left(\frac{\Phi_{zps}}{\varphi_0} \right)^2 (\hat{a}^\dagger + \hat{a})^2 - 2E_J \cos \left(\frac{\Phi_e}{\varphi_0} \right) \sum_n \frac{(-1)^n}{(2n)!} \left[\frac{\Phi_{zps}}{\varphi_0} (\hat{a}^\dagger + \hat{a}) \right]^{2n}. \quad (S13)$$

Following Ref. [1], for weak modulation depth $\delta f \approx \Phi_{zps}/\varphi_0$, we will keep only up to $\mathcal{O}(\Phi_{zps}^4)$ contributions in the Hamiltonian and expand the cosine potential to fourth order. Finally, going to rotating frame defined through $\hat{a} \rightarrow \hat{a} e^{-i\omega_p t/2}$, the Hamiltonian

reduces to

$$\hat{H} = -4E_C n_0^2 (\hat{a}^\dagger e^{i\omega_p t/2} - \hat{a} e^{-i\omega_p t/2})^2 + \left(\frac{E_L}{2} + E_J \cos\left(\frac{\Phi_e}{\varphi_0}\right) \right) \left(\frac{\Phi_{zps}}{\varphi_0} \right)^2 \left[\hat{a}^\dagger e^{i\omega_p t/2} + \hat{a} e^{-i\omega_p t/2} \right]^2 - \frac{E_J}{12} \cos\left(\frac{\Phi_e}{\varphi_0}\right) \left(\frac{\Phi_{zps}}{\varphi_0} \right)^4 \left[\hat{a}^\dagger e^{i\omega_p t/2} + \hat{a} e^{-i\omega_p t/2} \right]^4. \quad (\text{S14})$$

Using Jacobi-Anger expansion for $\cos(\Phi_e/\varphi_0)$ [2], and ignoring the higher orders of the Bessel function of $\delta f \ll 1$, following Ref. [2], we can rewrite the Hamiltonian as

$$\hat{H} = -4E_C n_0^2 (\hat{a}^\dagger e^{i\omega_p t/2} - \hat{a} e^{-i\omega_p t/2})^2 + \left(\frac{\Phi_{zps}}{\varphi_0} \right)^2 \left(\frac{E_L}{2} + E_J^{(0)} + E_J^{(1)} \cos(\omega_p t) + E_J^{(2)} \cos(2\omega_p t) \right) \left[\hat{a}^\dagger e^{i\omega_p t/2} + \hat{a} e^{-i\omega_p t/2} \right]^2 - \frac{1}{12} \left(\frac{\Phi_{zps}}{\varphi_0} \right)^4 (E_J^{(0)} + E_J^{(1)} \cos(\omega_p t) + E_J^{(2)} \cos(2\omega_p t)) \left[\hat{a}^\dagger e^{i\omega_p t/2} + \hat{a} e^{-i\omega_p t/2} \right]^4, \quad (\text{S15})$$

where, following Ref. [2], the Fourier coefficients are defined as $E_J^{(0)} = E_J J_0(\delta f) \cos F$, $E_J^{(1)} = -2E_J J_1(\delta f) \sin F$, $E_J^{(2)} = -2E_J J_2(\delta f) \cos F$, where J_m is the Bessel function of the m th order. For small amplitude of flux pump ($\delta f \ll 1$), these coefficients can be expressed as $E_J^{(0)} \approx E_J \cos F$, $E_J^{(1)} \approx -E_J \delta f \sin F$, and $E_J^{(2)} = -(E_J \delta f^2 \cos F)/4$ [2]. Ignoring the fast oscillating terms thorough RWA, we obtain the time-independent Hamiltonian

$$\hat{H}_{\text{STS}} = \Delta \hat{a}^\dagger \hat{a} + \frac{\lambda}{2} (\hat{a}^{\dagger 2} + \hat{a}^2) + K \hat{a}^{\dagger 2} \hat{a}^2 + \Lambda (\hat{a}^{\dagger 3} \hat{a} + \hat{a}^\dagger \hat{a}^3) + \zeta (\hat{a}^{\dagger 4} + \hat{a}^4), \quad (\text{S16})$$

where $\Delta = \omega_a - \omega_p/2 + 2K$, $\omega_a = \sqrt{8E_C(E_L + 2E_J \cos F)}$, $\lambda = E_J^{(1)} (\Phi_{zps}/\varphi_0)^2$, $K = -E_J^{(0)} (\Phi_{zps}/\varphi_0)^4/2$, $\Lambda = -E_J^{(1)} (\Phi_{zps}/\varphi_0)^4/6$, and $\zeta = -E_J^{(2)} (\Phi_{zps}/\varphi_0)^4/24$. In our simulations for the STS performance in the main text, we use $C_\Sigma = 4\text{pF}$, $L_J = 80\text{pH}$, and $L = 100\text{pH}$. While higher order Bessel functions and zero point flux fluctuations can be included in this analysis, based on these parameters and for modulation depth $\delta f \approx \Phi_{zps}/\varphi_0$, they are negligible. Similar to the SQUID case, Kerr nonlinearity is proportional to the $\cos F$, whereas the pumping strength λ and the extra nonideality Λ are proportional to $\sin F$. Just like flux-pumped JPA, we need to tune the static flux at $F = -\pi/2$ to cancel Kerr nonlinearity. Based on Eq. (S12), tuning the static flux at $F = -\pi/2$ will leave us with an LC oscillator, which is a linear resonator we can use for signal amplification. Therefore, unlike symmetric DC SQUID, we can operate STS at static flux $F = -\pi/2$ and cancel Kerr nonlinearity entirely while keeping the pumping term. Hence, we can write the static effective Hamiltonian for our STS design as

$$\hat{H}_{\text{STS}} = \Delta \hat{a}^\dagger \hat{a} + \frac{\lambda}{2} (\hat{a}^{\dagger 2} + \hat{a}^2) + \Lambda (\hat{a}^{\dagger 3} \hat{a} + \hat{a}^\dagger \hat{a}^3), \quad (\text{S17})$$

where $\Delta = \omega_a - \omega_p/2$, $\omega_a = \sqrt{8E_C E_L}$. The first two terms of the Hamiltonian correspond to the quantum-limited degenerate parametric amplifier (DPA), whereas the last term is the nonideality that deviates our amplifier from the quantum limit. However, the nonideality Λ is much smaller in amplitude than Kerr nonlinearity since $|\Lambda|/K = \delta f \tan F \ll 1$ for any static flux F . It is also much smaller than the pump strength in amplitude since $|\Lambda/\lambda| \propto (\Phi_{zps}/\varphi_0)^2 \ll 1$. Therefore, Kerr nonlinearity is the dominant nonideality that deviates the amplifier more from the quantum limit compared to Λ . Since STS with LC branch allows us to cancel K , our amplifier effectively operates at the quantum limit and is an improvement over the flux-pumped JPA's. In the case where the two SQUID loops are threaded asymmetrically where $\Phi_{1e} \neq \Phi_{2e}$ and $E_{J1} \neq E_{J2}$, the circuit Hamiltonian will also contain odd orders of Φ_{zps} . However, these odd orders vanish under RWA [1] and the form of the STS static effective Hamiltonian is maintained with redefined parameters, meaning that Kerr-free operation is still possible.

STS Design with Josephson Junctions

We now study the STS design discussed in Ref. [1] where the transmon branch consists of a Josephson junction J_2 with capacitance C_2 as shown in Fig. 7. Assuming $E_{J1} = E_{J2} = E_{J3} = E_J$, $\Phi_{1e} = \Phi_{2e} = \Phi_e$, and following Ref. [1], we can rewrite the Hamiltonian in Eq. (S12) as

$$\hat{H}_{\text{lab,STS}} = 4E_C \hat{n}^2 - E_J \cos\left(\frac{\tilde{\Phi}}{\varphi_0}\right) - 2E_J \cos\left(\frac{\Phi_e}{\varphi_0}\right) \cos\left(\frac{\tilde{\Phi}}{\varphi_0}\right), \quad (\text{S18})$$

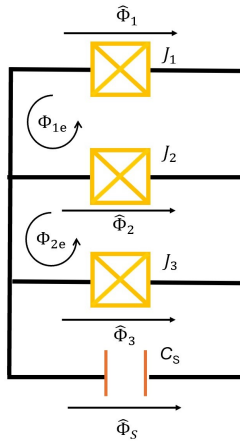


FIG. 7. STS design [1] shunted by capacitance C_S . The junctions J_1 and J_3 compose the “SQUID branch” whereas the junction J_2 gives the “transmon branch”. The loop between J_1 and J_2 is threaded by an external flux Φ_{1e} whereas the loop between J_2 and J_3 is threaded by an external flux Φ_{2e} . $\hat{\Phi}_{1,2,3,S}$ are the branch flux operators.

where $\varphi_0 = \hbar/2e$ is the reduced flux quantum, $\hat{n} = in_0(\hat{a}^\dagger - \hat{a})$ and $\tilde{\hat{\Phi}} = \Phi_{zps}(\hat{a}^\dagger + \hat{a})$, and Φ_{zps} is the zero point phase spread around the Josephson junction. Following the derivations in Ref. [1], the static effective STS Hamiltonian can be written in the same form as the Kerr-free STS amplifier

$$\hat{H}_{\text{STS}} = \Delta a^\dagger a + \frac{\lambda}{2}(\hat{a}^{\dagger 2} + \hat{a}^2) + K \hat{a}^{\dagger 2} \hat{a}^2 + \Lambda(\hat{a}^{\dagger 3} \hat{a} + \hat{a}^\dagger \hat{a}^3), \quad (\text{S19})$$

where the detailed definition of each coefficient can be found in Ref. [1]. However, unlike our STS design with the LC branch, the transmon branch in this design provides Kerr nonlinearity $K = -E_C/2$ which cannot be cancelled by static flux tuning. Therefore, having an LC branch is crucial for obtaining a Kerr-free amplifier.

HARMONIC BALANCE AND STABILITY DIAGRAM

We analyze the Quantum Langevin equation (QLE) for mode \hat{a} derived from the input-output theory [4]

$$\dot{\hat{a}} = i[\hat{H}_{\text{STS}}, \hat{a}] - \frac{\kappa}{2}\hat{a} + \sqrt{\kappa}\hat{a}_{\text{in}}, \quad (\text{S20})$$

where κ is the cavity decay rate and the static effective Hamiltonian \hat{H}_{STS} is defined in the main text. We treat the input and output fields as classical drives $\alpha_{\text{in(out)}} = \sum_x \alpha_x e^{-i\omega_x t}$ where $\omega_x = m\omega_p + n\omega_s$ represents all possible harmonics, with m, n being integer values. To solve the QLE, we apply the semiclassical harmonic balance solution

$$\alpha(t) = \langle \alpha | \hat{a}(t) | \alpha \rangle = \sum_{\omega=-\omega_x}^{\omega_x} \alpha(\omega) e^{-i\omega t}, \quad (\text{S21})$$

which runs over all the harmonics mentioned before. This can be expressed as

$$\alpha(t) = \sum_{\omega=0}^{\omega_x} \left(\alpha(\omega) e^{-i\omega t} + \alpha(-\omega) e^{i\omega t} \right). \quad (\text{S22})$$

We can express the second term in the sum as a positive frequency Fourier component. For that, we first look into the relation between the flux and charge operators $\hat{\Phi} = \hat{Q}/C_c$, where $\hat{\Phi} = \Phi_{zps}(\hat{a} + \hat{a}^\dagger)$, $\hat{Q} = iq_{zps}(\hat{a}^\dagger - \hat{a})$, and C_c is the capacitance of our lumped-element amplifier circuit. Based on the Fourier transform

$$\hat{a}(t) = \frac{1}{\sqrt{2\pi}} \int_{-\infty}^{\infty} \bar{a}[\omega] e^{-i\omega t} d\omega, \quad (\text{S23})$$

$$\bar{a}[\omega] = \frac{1}{\sqrt{2\pi}} \int_{-\infty}^{\infty} \hat{a}(t) e^{i\omega t} dt, \quad (\text{S24})$$

where $\bar{a}[\omega]$ is the Fourier transform of the annihilation operator. We can then say that $\hat{\Phi} = -i\omega\hat{a}$. Using the relation between the flux and charge operators discussed above, we express the relation between the creation and annihilation operator as

$$\hat{a}^\dagger(t) = \frac{\omega_c - \omega}{\omega_c + \omega} \hat{a}(t), \quad (\text{S25})$$

where $\omega_c = q_{\text{zps}}/(C_c \Phi_{\text{zps}})$ is the cavity resonance frequency. Then the relation between the negative frequency Fourier component of the annihilation operator and the positive frequency Fourier component of the creation operator is given by

$$\bar{a}^\dagger[-\omega] = \frac{\omega_c - \omega}{\omega_c + \omega} \bar{a}[\omega]. \quad (\text{S26})$$

Taking the Hermitian conjugate of this expression, we get

$$\bar{a}[-\omega] = \frac{\omega_c - \omega}{\omega_c + \omega} \bar{a}^\dagger[\omega]. \quad (\text{S27})$$

Then we can rewrite second term inside the sum in Eq. (S22), and get

$$\alpha(t) = \sum_{\omega=0}^{\omega_x} \left(\alpha(\omega) e^{-i\omega t} + \frac{\omega_c - \omega_x}{\omega_c + \omega_x} \alpha^*(\omega) e^{i\omega t} \right). \quad (\text{S28})$$

For the rest of the paper, we will use the notation $\alpha_x = \alpha(\omega_x)$. We neglect the out-of-band harmonics, and only take into account the harmonics at frequencies ω_s , ω_i , and $\omega_p/2$. Since we assume that these harmonics are in resonance with the cavity frequency, the second term of the harmonic balance solution vanishes. The equation of motion in Eq. (S47) is reduced to three equations for the amplitudes of these harmonics (α_s , α_i , and α_h respectively) as follows:

$$(\omega - \Delta + i\frac{\kappa}{2})\alpha_s = i\sqrt{\kappa}\alpha_{\text{in},s} + \lambda\alpha_i^* + 3\Lambda[(|\alpha_i|^2 + 2|\alpha_s|^2 + 2|\alpha_h|^2)\alpha_i^* + (\alpha_h^2 + \alpha_h^{*2} + \alpha_i\alpha_s)\alpha_s], \quad (\text{S29})$$

$$(-\omega - \Delta + i\frac{\kappa}{2})\alpha_i = i\sqrt{\kappa}\alpha_{\text{in},i} + \lambda\alpha_s^* + 3\Lambda[(|\alpha_s|^2 + 2|\alpha_i|^2 + 2|\alpha_h|^2)\alpha_s^* + (\alpha_h^2 + \alpha_h^{*2} + \alpha_i\alpha_s)\alpha_i], \quad (\text{S30})$$

$$(-\Delta + i\frac{\kappa}{2})\alpha_h = i\sqrt{\kappa}\alpha_{\text{in},h} + \lambda\alpha_h^* + 3\Lambda[(|\alpha_h|^2 + 2|\alpha_s|^2 + 2|\alpha_i|^2)\alpha_h^* + [2(\alpha_i\alpha_s + \alpha_i^*\alpha_s^*) + \frac{1}{3}\alpha_h^2]\alpha_h], \quad (\text{S31})$$

where $\omega = \omega_s - \omega_p/2$ is the signal detuning, and $\alpha_{\text{in},s}$, $\alpha_{\text{in},i}$, and $\alpha_{\text{in},h}$ are the classical drive strengths at corresponding harmonics. To determine the stability regions of our amplifier, we solve for the cavity amplitude α_h in Eq. (S31). We assume small-signal approximation where the terms $|\alpha_s|^2$, $|\alpha_i|^2$, $\alpha_i\alpha_s$, and $\alpha_i^*\alpha_s^*$ can be neglected. Since there is no input drive at frequency $\omega_p/2$, we take $\alpha_{\text{in},h} = 0$. Then Eq. (S31) is simplified as

$$(-\Delta + i\frac{\kappa}{2} - \Lambda\alpha_h^2)\alpha_h = (\lambda + 3\Lambda|\alpha_h|^2)\alpha_h^*. \quad (\text{S32})$$

We can express α_h as $\alpha_h = x + iy$, where $x = \text{Re}(\alpha_h)$ and $y = \text{Im}(\alpha_h)$. Substituting this into Eq. (S32), we can write the real part of the whole expression as

$$4\Lambda x^3 + (\lambda + \Delta)x + \frac{\kappa}{2}y = 0, \quad (\text{S33})$$

and the imaginary part as

$$4\Lambda y^3 + (\lambda - \Delta)y + \frac{\kappa}{2}x = 0. \quad (\text{S34})$$

We can see that in the limit where $\Lambda = 0$, we obtain a system of linear equations with solution $(x, y) = (0, 0)$, which corresponds to the case of a DPA.

To solve the system of nonlinear equations in general, we can uncouple the equations into two ninth-order polynomials. This results several different possible pairs of solutions depending on the values of λ and Δ : one solution, three solutions, five solutions, seven solutions, and nine solutions. We note that for all λ and Δ values, the trivial solution $(x, y) = (0, 0)$ is always a

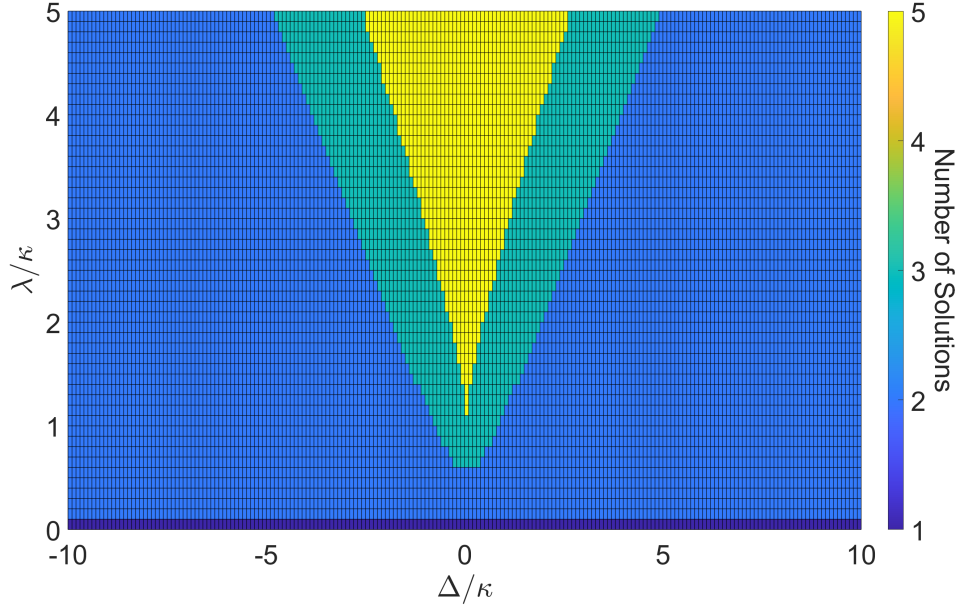


FIG. 8. The stability diagram of the Kerr-free STS amplifier for various drive and detuning values. The case of four stable $|\alpha_h|^2$ values occur right at the border of the tri-stable and penta-stable regions.

solution. We also further note that if $(x, y) = (r_1, r_2)$ is a non-trivial solution to the coupled equations, then $(x, y) = (-r_1, -r_2)$ is also a solution. Since the number of stable points is equivalent to the number of unique $|\alpha_h|^2$ solutions, we can conclude that (r_1, r_2) and $(-r_1, -r_2)$ give the same $|\alpha_h|^2$ solution, since $|\alpha_h|^2 = x^2 + y^2 = r_1^2 + r_2^2 = (-r_1)^2 + (-r_2)^2$. This leads us to conclude that the number of possible stable $|\alpha_h|^2$ values is between one and five depending on the values of λ and Δ . The number of stable points can be plotted in a stability diagram as a function of λ and Δ .

We find that the transition between the bi-stable and tri-stable region is given by the condition $\lambda^2 - \Delta^2 = \kappa^2/4$.

For the region where $\lambda/\kappa < 0.5$, there is only bistability. Despite that, we can still treat the STS amplifier as effectively mono-stable because of how far apart the two stable points are, as shown in Figure 9. Since amplifiers usually only operate at the trivial point as in the case of the DPA, as long as the photon number is small we do not have to be concerned with the other stable point coming into play.

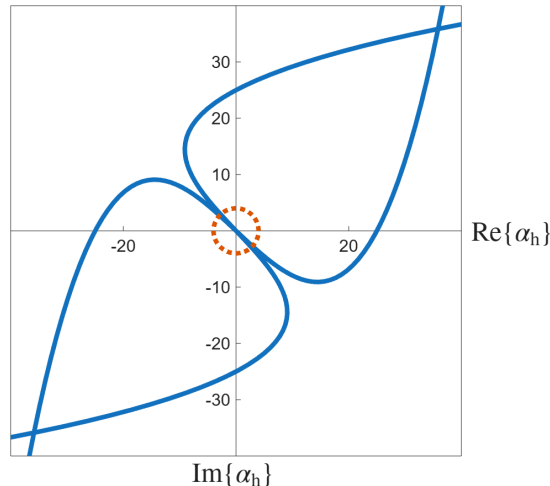


FIG. 9. The stable points of α_h for $\Delta = 0$ and $|\lambda| = 0.472631\kappa$. The intersection of the blue plots are the solutions to the coupled equations and $|\alpha_h|^2$ is the distance from the origin to the intersection point. This corresponds to the bistable regime, since there are two unique $|\alpha_h|^2$ values. The dashed circle is the typical total photon number in the Kerr-free STS amplifier, which is far away from the nontrivial intersection points. Therefore, the STS amplifier can be treated as an effective mono-stable system.

ANALYTICAL GAIN EXPRESSION

To derive the phase-preserving gain analytically, we evaluate the coupled equations of the single-SQUID JPA and then obtain the results for STS amplifier for $K = 0$. Under the assumption that we can operate an amplifier at $\alpha_h = 0$, as discussed in previous section, we can rewrite these equations as

$$\left(\omega - (\Delta + 2K(2|\alpha_i|^2 + |\alpha_s|^2) + 3\Lambda\alpha_i\alpha_s) + i\frac{\kappa}{2} \right) \alpha_s = i\sqrt{\kappa}\alpha_{in,s} + (\lambda + 3\Lambda(|\alpha_i|^2 + 2|\alpha_s|^2))\alpha_i^*, \quad (S35)$$

$$\left(-\omega - (\Delta + 2K(|\alpha_i|^2 + 2|\alpha_s|^2) + 3\Lambda\alpha_i\alpha_s) + i\frac{\kappa}{2} \right) \alpha_i = i\sqrt{\kappa}\alpha_{in,i} + (\lambda + 3\Lambda(|\alpha_s|^2 + 2|\alpha_i|^2))\alpha_s^*. \quad (S36)$$

For large gain ($G \gg 1$), we can assume that $n_s \approx n_i$ where $n_{s,i} = |\alpha_{s,i}|^2$ [5]. Then, we can rewrite these equations as

$$\left(\omega - \Delta_{eff} + i\frac{\kappa}{2} \right) \alpha_s = i\sqrt{\kappa}\alpha_{in,s} + \lambda_{eff}\alpha_i^*, \quad (S37)$$

$$\left(-\omega - \Delta_{eff}^* - i\frac{\kappa}{2} \right) \alpha_i^* = -i\sqrt{\kappa}\alpha_{in,i}^* + \lambda_{eff}^*\alpha_s, \quad (S38)$$

where $\Delta_{eff} = \Delta + 6Kn_s + 3\Lambda\alpha_i\alpha_s$, and $\lambda_{eff} = \lambda + 9\Lambda n_s$, and we have taken the complex conjugate of the equation for the idler harmonic. The effective detuning and squeezing drive contain corrections from the nonidealities K and Λ . Let us express the coefficients with letters A and B such that

$$A\alpha_s - \lambda_{eff}\alpha_i^* = i\sqrt{\kappa}\alpha_{in,s}, \quad (S39)$$

$$B\alpha_i^* - \lambda_{eff}^*\alpha_s = -i\sqrt{\kappa}\alpha_{in,i}^*. \quad (S40)$$

Then we can write α_i^* in terms of α_s , and vice versa, and then express the matrix equation between the signal and idler amplitudes and input field amplitudes

$$\begin{pmatrix} \alpha_s \\ \alpha_i^* \end{pmatrix} = i\sqrt{\kappa} \begin{pmatrix} 1/D_1 & \lambda_{eff}/(BD_1) \\ \lambda_{eff}^*/(AD_2) & -1/D_2 \end{pmatrix} \begin{pmatrix} \alpha_{in,s} \\ \alpha_{in,i}^* \end{pmatrix}, \quad (S41)$$

where $D_1 = A - |\lambda_{eff}|^2/B$, and $D_2 = B - |\lambda_{eff}|^2/A$. For each harmonics, we use the input output relation [4]

$$\alpha_{out} = \sqrt{\kappa}\alpha - \alpha_{in}. \quad (S42)$$

Then, we can write the matrix for the input and output fields as

$$\begin{pmatrix} \alpha_{out,s} \\ \alpha_{out,i}^* \end{pmatrix} = i\kappa \begin{pmatrix} 1/D_1 & \lambda_{eff}/(BD_1) \\ \lambda_{eff}^*/(AD_2) & -1/D_2 \end{pmatrix} \begin{pmatrix} \alpha_{in,s} \\ \alpha_{in,i}^* \end{pmatrix} - \begin{pmatrix} 1 & 0 \\ 0 & 1 \end{pmatrix} \begin{pmatrix} \alpha_{in,s} \\ \alpha_{in,i}^* \end{pmatrix}. \quad (S43)$$

The signal gain is expressed as

$$G_s = \left| \frac{\alpha_{out,s}}{\alpha_{in,s}} \right|^2 = \left| \frac{i\kappa (\omega + \Delta_{eff}^* + i\frac{\kappa}{2})}{(\omega - \Delta_{eff} + i\frac{\kappa}{2}) (\omega + \Delta_{eff}^* + i\frac{\kappa}{2}) + |\lambda_{eff}|^2} - 1 \right|^2. \quad (S44)$$

This is effectively the same gain expression as DPA, as discussed in [2]. For the STS amplifier, we take $K = 0$, which has smaller corrections to the detuning compared to single-SQUID JPA's and is therefore closer to a DPA.

Normalizing the Added Noise

For our simulations in phase-preserving quantum efficiency, we note that while the added noise number \mathcal{A} is unitless and represents the photon number, the input-output relation in Eq. (S42) suggests that the second-moment noises are in units of frequency. We therefore need to normalize the second-order noises so that they are in units of photon numbers.

As discussed in [2, 6], for degenerate signal and idler inputs ($\omega_s = \omega_i$), we can write the added noise operator in terms of the input idler field \hat{a}_{in}^\dagger and write the input-output relation as

$$\hat{a}_{out} = g\hat{a}_{in} + \sqrt{|g|^2 - 1}\hat{a}_{in}^\dagger, \quad (S45)$$

where g is the signal amplitude gain, and $\omega = \omega_s - \omega_p/2$. Then, based on [7], the added noise can be defined in terms of the idler noise

$$\mathcal{A} = \frac{G-1}{G} \langle |\Delta \hat{a}_{\text{in}}|^2 \rangle, \quad (\text{S46})$$

where $G = |g|^2$ is the phase-preserving signal gain. Based on the relation $\mathcal{A} \geq (1 - 1/G)/2$ derived in [7], we know that a quantum-limited DPA should satisfy the lower bound of the added noise number. Hence idler noise $\langle |\Delta \hat{a}_{\text{in}}|^2 \rangle = 1/2$ is in units of photon number. To express idler noise analytically, we first express the input field analytically, using the QLE

$$\dot{\hat{a}} = i[\hat{H}_{\text{DPA}} + \hat{H}_{\text{probe}}, \hat{a}] - \frac{\kappa}{2} \hat{a} + \sqrt{\kappa} \hat{a}_{\text{in}}. \quad (\text{S47})$$

Then, we express the input field in terms of the intracavity field operators in steady state

$$\hat{a}_{\text{in}} = \frac{1}{\sqrt{\kappa}} \left[\left(-i\omega + i\Delta + \frac{\kappa}{2} \right) \hat{a} + i\lambda \hat{a}^\dagger + i\epsilon_{\text{probe}} \right]. \quad (\text{S48})$$

Since our simulations are done at center frequency $\omega = 0$ where signal is resonant with the cavity, the noise in vacuum is

$$\langle |\Delta \hat{a}_{\text{in}}|^2 \rangle = \langle 0 | |\Delta \hat{a}_{\text{in}}|^2 | 0 \rangle = \frac{1}{2} \left(\frac{\kappa}{4} + \frac{|\lambda|^2}{\kappa} \right). \quad (\text{S49})$$

Since we know the added noise for DPA at high gain is half a photon, we normalize the noise by a drive-dependent frequency of $(\kappa/4 + |\lambda|^2/\kappa)$. When calculating the added noise for JPAs and STS, we similarly derive \hat{a}_{in} from QLE and calculate the noise $\langle |\Delta \hat{a}_{\text{in}}|^2 \rangle$ analytically. We then calculate \mathcal{A} by simulating the phase-preserving gain G by sweeping λ . Finally, we normalize \mathcal{A} by $(\kappa/4 + |\lambda_{\text{DPA}}|^2/\kappa)$, where λ_{DPA} is the two-photon drive strength applied on DPA that corresponds to the gain of the given JPA or STS, which we can calculate from the analytical gain expression derived in [2].

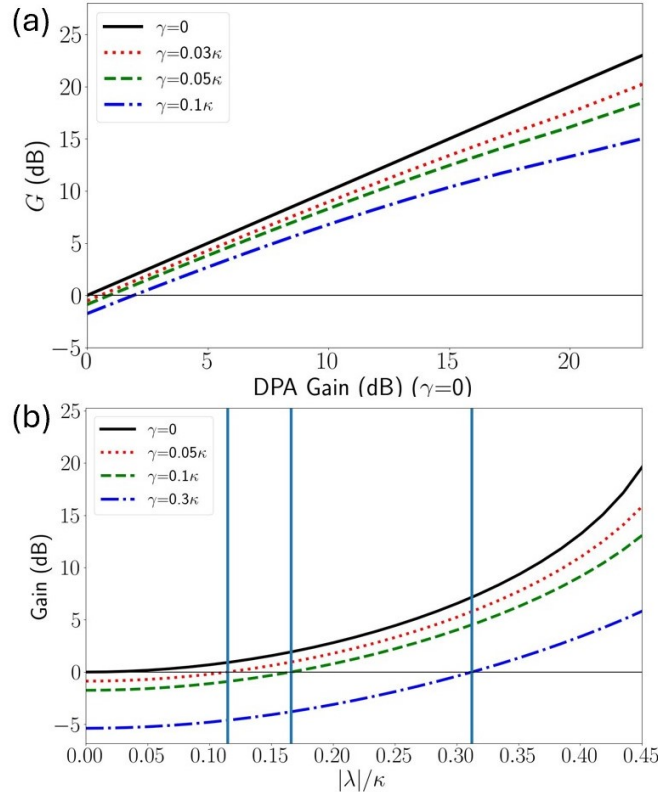


FIG. 10. (a) STS amplifier phase-preserving gain against DPA gain without additional loss rate γ . (b) STS amplifier phase-preserving gain against two-photon drive strength λ for various coupling rates γ due to undesirable additional vacuum noise mixed to the signal. Vertical lines represent the λ necessary to mitigate deamplification for each plot, derived from the analytical DPA gain in [2]. For both figures $\kappa = 300\text{MHz}$, $\Delta = \omega = 0$.

Extra Noise

In this paper we have assumed a lossless parametric amplifier, where the damping rate of the cavity only consists of κ due to coupling the signal to be amplified. However, in experiments there are undesired losses in the resonator that mix additional vacuum noise to the signal [2]. We can treat these losses as an additional input port coupled to the cavity with an input field \hat{b}_{in} and coupling rate γ . The total damping rate for the STS amplifier is then $\bar{\kappa} = \kappa + \gamma$ and the QLE is written as

$$\dot{\hat{a}} = i[\hat{H}_{\text{STS}}, \hat{a}] - \frac{\bar{\kappa}}{2}\hat{a} + \sqrt{\kappa}\hat{a}_{\text{in}} + \sqrt{\gamma}\hat{b}_{\text{in}}. \quad (\text{S50})$$

In Fig. 10(a), we show that a lossless ($\gamma = 0$) Kerr-free STS amplifier is performing like a DPA, as seen in our previous phase-preserving gain results. However, when there is extra noise mixing with the signal due to undesired losses ($\gamma > 0$), the STS amplifier deviates from DPA and gain decreases with increasing γ . We further note that extra damping due to γ leads to deamplification as we see gain below zero. In Fig. 10(b) we show how much two-photon drive strength λ is necessary to mitigate the deamplification of the STS under various damping rates of γ . It shows that increasing damping rate γ deamplifies the signal more and requires stronger two-photon drive to be mitigated. The zero gain threshold for the drive strengths in this figure have been calculated from the analytical gain expression for DPA. As discussed in Ref. [2], the signal gain for DPA with extra loss can be derived from the input-output relation in Fourier space

$$\overline{\hat{a}_{\text{out}}}[\omega] = g_{S,\omega}\overline{\hat{a}_{\text{in}}}[\omega] + g_{I,\omega}\overline{\hat{a}_{\text{in}}}^\dagger[-\omega] + \sqrt{\frac{\gamma}{\kappa}} \left[(g_{S,\omega} + 1)\overline{\hat{b}_{\text{in}}}[\omega] + g_{I,\omega}\overline{\hat{b}_{\text{in}}}^\dagger[-\omega] \right], \quad (\text{S51})$$

where $g_{S,\omega}$ is the signal amplitude gain and $g_{I,\omega}$ is the idler amplitude gain. The DPA amplitude gain is expressed as

$$g_{S,\omega} = \frac{\kappa\bar{\kappa}/2 - i\kappa(\Delta + \omega)}{\Delta^2(\bar{\kappa}/2 - i\omega)^2 - |\lambda|^2} - 1 \quad (\text{S52})$$

We see that the DPA gain results match exactly with the drive strengths at which STS gain is zero. This shows that our lossy STS amplifier operates at lossy DPA level performance.

* Correspondence should be addressed to: bbhandari@chapman.edu

- [1] B. Bhandari, I. Huang, A. Haja, K. Yanik, B. Qing, K. Wang, D. I. Santiago, J. Dressel, I. Siddiqi, and A. N. Jordan, *PRX Quantum* **6**, 030338 (2025).
- [2] S. Boutin, D. M. Toyli, A. V. Venkatramani, A. W. Eddins, I. Siddiqi, and A. Blais, *Phys. Rev. Appl.* **8**, 054030 (2017).
- [3] X. You, J. A. Sauls, and J. Koch, *Phys. Rev. B* **99**, 174512 (2019).
- [4] D. Walls and G. J. Milburn, in *Quantum optics*, edited by G. J. Milburn (Springer, 2008) pp. 307–346.
- [5] N. E. Frattini, V. V. Sivak, A. Lingenfelter, S. Shankar, and M. H. Devoret, *Phys. Rev. Appl.* **10**, 054020 (2018).
- [6] A. Roy and M. Devoret, *Comptes Rendus Physique* **17**, 740 (2016).
- [7] C. M. Caves, J. Combes, Z. Jiang, and S. Pandey, *Phys. Rev. A* **86**, 063802 (2012).